TABLE 1. COMPARISON OF VERTEBRAL MICROSTRUCTURAL PARAMETERS BETWEEN TWO GROUPS WITHOUT AND WITH FRACTURE

	Without fracture (n = 43)	*With fracture (n = 39)*	*p (by t-test)*
Background data			
Anthropometric data			
Age (years)	64.4 ± 5.5	66.2 ± 3.8	NS
Age at menopause (years)	50.3 ± 2.8	48.9 ± 4.2	NS
Body height (cm)	152.3 ± 4.7	150.1 ± 7.2	NS
Body weight (kg)	52.8 ± 7.3	50.1 ± 7.8	NS
Areal BMD by DXA (g/cm^2)	0.925 ± 0.161	0.836 ± 0.191	0.05
MDCT data			
Microstructure parameters			
App BV/TV (%)	36.1 ± 7.0	26.1 ± 8.5	<0.0001
App Tb.N ($1/mm^3$)	0.97 ± 0.09	0.78 ± 0.20	<0.0001
App Tb.Th (μm)	368.3 ± 46.1	335.8 ± 46.2	0.005
App Tb.Sp (μm)	667 ± 129	1064 ± 439	<0.0001
Structure model index	1.87 ± 0.48	2.70 ± 0.38	<0.0001
Euler's number	−1037 ± 375	−457 ± 404	<0.0001
Fractal dimension	2.52 ± 0.06	2.41 ± 0.18	0.0005
Degree of anisotropy	1.44 ± 0.15	1.58 ± 0.35	0.05
Volumetric BMD (mg/cm^3)	103.9 ± 23.5	72.0 ± 18.5	<0.0001

Data are shown as mean ± SD.

app BV/TV, apparent bone volume fraction; app Tb.N, apparent trabecular number; app Tb.Th, apparent trabecular thickness; app Tb.Sp, apparent trabecular separation; NS, not significant.

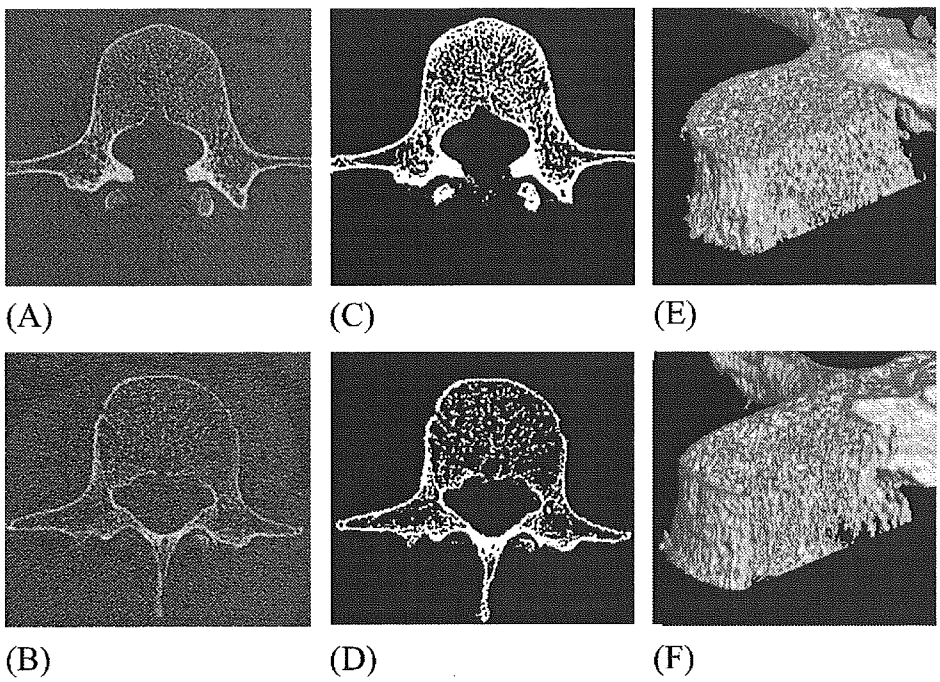

FIG. 4. Representative 2D and 3D MDCT images of the third lumbar spine. (A and B) 2D and (E and F) 3D MDCT images of the third lumbar spine were obtained from (A and E) a 62-year-old woman without vertebral fracture and (B and F) a woman of the same age with a vertebral fracture in her thoracic spine. (C and D) Binarized images are also shown.

trabeculae (app Tb.N: 0.97 versus 0.78), more rodlike structure (SMI: 1.87 versus 2.70), and lower connectivity (Euler's number: −1037 versus −457). The ORs of microstructure parameters, such as SMI, Euler's number, and app BV/TV, for association with prevalent fracture were much higher than that ratio for association of areal BMD by DXA with it. SMI and Euler's number, which represent nonmetric features of trabecular structure, would seem to be more useful than metric parameters such as app Tb.N, app Tb.Th, or app Tb.Sp. It is an advantage of the MDCT scanning system that, in addition to assessing these 3D microstructure parameters, volumetric BMD values can be obtained at the same time by using a reference phantom; these values correlate highly with the presence of fracture.

In vivo analysis of trabecular microstructure has been studied using conventional radiography, high-resolution CT, and high-resolution MRI. Conventional radiography has a spatial resolution of up to 40 μm; however, it delivers projectional images of the trabecular structure. Conventional high-resolution CT with spatial resolution of 400 μm shows only structural texture, because the trabecular structure is subjected to partial-volume effects. With the use of

TABLE 2. CORRELATIONS BETWEEN MICROSTRUCTURAL PARAMETERS AND BMD

Structure parameters by MDCT	*Volumetric BMD by QCT*		*Areal BMD by DXA*	
	R^2	*p*	R^2	*p*
App BV/TV (%)	0.645	0.0001	0.128	0.005
Structure model index	0.514	0.0001	0.151	0.0005
App Tb.Th (μm)	0.487	0.0001	0.083	0.01
Euler's number	0.433	0.0001	0.125	0.005
App Tb.N (1/mm^3)	0.428	0.0001	0.104	0.005
App Tb.Sp (μm)	0.350	0.0001	0.045	NS
Fractal dimension	0.311	0.0001	0.213	0.0001
Degree of anisotropy	0.084	0.01	0.034	NS

app BV/TV, apparent bone volume fraction; app Tb.Th, apparent trabecular thickness; app Tb.N, apparent trabecular number; app Tb.Sp, apparent trabecular separation; NS, not significant.

TABLE 3. ROC ANALYSIS AND ORS OF MICROSTRUCTURAL PARAMETERS FOR THEIR ASSOCIATION WITH SPINAL FRACTURE

Measurements	*AUC (ROC)*	*p*	*OR (95% CI)*	*p*
MDCT				
Microstructural parameters				
Structural model index	0.928 ± 0.027	0.0001	16.0 (5.3–48.4)	0.0001
App BV/TV (%)	0.811 ± 0.048	0.0001	13.6 (4.3–42.4)	0.0001
Euler's number	0.857 ± 0.043	0.0001	13.1 (4.5–38.1)	0.0001
App Tb.Sp (μm)	0.818 ± 0.048	0.0001	7.4 (2.8–19.8)	0.0001
Fractal dimension	0.735 ± 0.059	0.0001	7.4 (2.6–20.7)	0.0005
App Tb.N (1/mm^3)	0.810 ± 0.049	0.0001	6.6 (2.5–17.4)	0.0005
App Tb.Th (μm)	0.674 ± 0.059	0.01	5.5 (1.6–18.5)	0.01
Degree of anisotropy	0.627 ± 0.063	0.05	3.5 (1.2–10.2)	0.05
Volumetric BMD (mg/cm^3)	0.870 ± 0.040	0.0001	12.7 (4.4–36.4)	0.0001
DXA areal BMD (g/cm^2)	0.647 ± 0.062	0.05	4.8 (1.5–14.8)	0.05

Data are shown as mean ± SD.
app BV/TV, apparent bone volume fraction; app Tb.Sp, apparent trabecular separation; app Tb.N, apparent trabecular number; app Tb.Th, apparent trabecular thickness.

TABLE 4. CORRELATION OF MICROSTRUCTURE PARAMETERS AND BMD WITH FRACTURE

vBMD with microstructure parameters			*aBMD with microstructure parameters*		
Measures	R^2	*p*	*Measures*	R^2	*p*
vBMD	0.366	0.0001	aBMD	0.061	0.0251
SMI	0.486	0.0001	SMI	0.486	0.0001
Tb.Th	0.112	0.0021	Euler's number	0.362	0.0001
vBMD + SMI	0.508	0.0001	aBMD + SMI	0.486	0.0001
vBMD + SMI + Tb.T	0.551	0.0001	aBMD + SMI + Euler's number	0.506	0.0001

Correlation with prevalent vertebral fracture was assessed by multivariate regression analysis.
vBMD, volumetric BMD; aBMD, areal BMD.

high-resolution CT in vivo, analysis of trabecular structure such as connectivity from a skeletonized representation of the trabecular network,[4] parameters derived from run-length encoding,[6] and number or area of holes in trabecular structure[15] have been reported. Their images had a slice thickness of 1.5 mm and the FOV was reduced to yield an image matrix with a pixel size of 0.31 mm. A good relationship between texture parameters calculated from high-resolution CT images and biomechanical properties has also been reported.[5] However, this spatial resolution only provides characteristics of trabecular structure, and 2D image has limited reproducibility among follow-up examinations.

With the recent advances in MRI hardware and software, it has become possible to obtain higher resolution MR images of trabecular bone[16–22] with in-plane resolutions as high as 150 μm and slice thicknesses of 280 μm in vivo.[23] MRI has an advantage of nonionization, and trabecular microstructure obtained in vivo by using high-resolution MR has been shown to be useful in predicting prevalent spinal fractures. Structural parameters of the distal radius with a 3D spin-echo sequence (voxel size of 137 × 137 × 500 μm^3) in 36 female patients were reported to provide a better index than the BMD of the distal radius.[24] 3D gradient-echo sequence (voxel size of 156 × 156 × 500 μm^3) could discriminate between groups with and without a recent hip

TABLE 5. CORRELATIONS OF MICROSTRUCTURAL PARAMETERS BY MDCT WITH AGE OR BODY WEIGHT

	Vs. age (years)		*Vs. body weight (kg)*	
	R^2	*p*	R^2	*p*
Microstructure parameters				
App BV/TV (%)	0.114	0.0005	0.029	NS
App Tb.N (1/mm^3)	0.122	0.005	0.147	0.0005
App Tb.Th (μm)	0.099	0.005	0.030	NS
App Tb.Sp (μm)	0.081	0.01	0.125	0.005
Structure model index	0.181	0.0001	0.048	0.05
Euler's number	0.185	0.0001	0.068	0.05
Fractal dimension	0.049	0.05	0.030	NS
Degree of anisotropy	0.005	NS	0.130	0.001
BMD				
Areal BMD by DXA (g/cm^2)	0.091	0.01	0.072	0.05
Volumetric BMD by MDCT (mg/cm^3)	0.118	0.005	0.001	NS

app BV/TV, apparent bone volume fraction; app Tb.N, apparent trabecular number; app Tb.Th, apparent trabecular thickness; app Tb.Sp, apparent trabecular separation; NS, not significant.

fracture.[21] A disadvantage of high-resolution MRI in vivo, however, is the relatively long acquisition time of up to 10 ± 20 minutes. A small FOV is required to obtain a high signal-to-noise ratio in the fast gradients with optimized coils. Because of these prerequisites and motion artifacts in the axial skeleton, application of high-resolution MRI is currently limited to peripheral sites such as phalanges, calcaneus, and distal radius.[19,20,25–27] Vertebral fracture is the most common osteoporotic fracture, and the presence of fracture indicates a greater risk for future fracture, independently of BMD.[28] The direct assessment of vertebral microstructure, as reported here, can be expected to provide greater sensitivity for assessing the risk of spinal fracture.

To our knowledge, there has been no report on in vivo analysis of microstructure by MDCT. Several specimen studies showed the capability to depict microstructure by MDCT in comparison with contact radiography[16] or μCT.[17] Although MDCT is the only available technique to analyze vertebral microstructure in vivo, high radiation exposure cannot be avoided. The radiation dose for DXA is small (0.08 ± 4.6 mSv). Fan beam DXA with increased resolution requires an increased radiation dose (6.7 ± 31 mSv), but this dose is smaller than that for QCT (25 ± 360 mSv).[29] In a study comparing radiation doses between single-detector row CT and MDCT, a 28% higher radiation dose was needed within the scanned volume for the latter at a constant noise level.[30] In this study, we evaluated the image quality of trabecular microstructure as a function of radiation exposure dose by using excised human vertebrae. Within the limits of clinically available radiation sets, MDCT at 300 mAs provided the best image quality and showed the highest correlation with the μCT data. As the reference level for CT examination of the abdomen (CTDIw) of adult patients is 35 mGy (according to European Commission 1999), the CTDIw for our current MDCT scanning at 300 mAs was 77.1 mGy. This radiation dose would be acceptable for a once-a-year study on postmenopausal women. On further advancement of the technology, a reduction in the radiation dose and higher resolution with a higher signal-to-noise ratio would be expected to make this method an even more useful diagnostic tool. In fact, the CTDIw for a new 16-detector row CT apparatus is 19.7 mGy, and advanced CT technology is expected to provide higher-resolution CT images. In the future, finite element analysis (FEA) may also be applied to 3D MDCT data for assessment of biomechanical properties,[31,32] and together this combination should provide a powerful tool for early evaluation of fracture risk.

In conclusion, 3D imaging of trabecular microstructure can be performed by using clinical MDCT at a high spatial resolution, and microstructure parameters derived from these images, especially those related to the shape of trabecular structures and connectivity, are more useful than spinal DXA for the assessment of fracture risk.

ACKNOWLEDGMENTS

The authors thank Tomoko Nakata and Takako Shimogama (Division of Radiology, Nagasaki University Hospital) and Jun Kono (Department of Radiology, Nagasaki Saiseikai Hospital) for CT scanning and analysis of trabecular structure. This work was supported in part by the Program for Promotion of Fundamental Studies in Health Science from Pharmaceuticals and Medical Device Agency (Pmda) of Japan (MF-14 to MI) and by a Health and Labour Sciences Research Grant (Comprehensive Research on Aging and Health) from the Ministry of Health, Labour and Welfare of Japan (to MI and HO).

REFERENCES

1. Siris ES, Chen Y-T, Abbott TA, Barrett-Connor E, Miller PD, Wehren LE, Berger MC 2004 Bone mineral density thresholds for pharmacological intervention to prevent fractures. Arch Intern Med **164:**1108–1112.
2. Riggs BL, Melton LJ 2002 Bone turnover matters: The raloxifene treatment paradox of dramatic decreases in vertebral fractures without commensurate increases in bone density. J Bone Miner Res **17:**11–14.

3. Seeman E 2002 Pathogenesis of bone fragility in women and men. Lancet **359:**1841–1850.
4. Chevalier F, Laval-Jeantet A, Laval-Jeantet M, Bergot C 1992 CT image analysis of the vertebral trabecular network in vivo. Calcif Tissue Int **51:**8–13.
5. Link TM, Majumdar S, Lin J, Augat P, Gould R, Newitt D, Ouyang X, Lang T, Mathur A, Genant HK 1998 Assessment of trabecular structure using high-resolution CT images and texture analysis. J Comput Assist Tomogr **22:**15–24.
6. Ito M, Ohki M, Hayashi K, Yamada M, Uetani M, Nakamura T 1995 Trabecular texture analysis of CT images in the relationship with spinal fracture. Radiology **194:**55–59.
7. Ruegsegger P, Koller B, Mueller R 1996 A microtomographic system for the non-destructive evaluation of bone architecture. Calcif Tissue Int **58:**24–29.
8. Mueller R, Hahn M, Vogel M, Delling G, Ruegsegger P 1996 Morphometric analysis of non-invasively assessed bone biopsies: Comparison of high-resolution computed tomography and histologic sections. Bone **18:**215–220.
9. Hildebrand T, Ruegsegger P 1997 A new method for the model-independent assessment of thickness in three-dimensional images. J Microsc **185:**67–75.
10. Parfitt AM, Drezner MK, Glorieux FH, Kanis JA, Malluche H, Meunier PJ, Ott SM, Recker RR 1987 Bone histomorphometry: Standardization of nomenclature, symbols, and units. Report of the ASBMR Histomorphometry Nomenclature Committee. J Bone Miner Res **2:**595–610.
11. Fazzalari NL, Parkinson IH 1996 Fractal dimension and architecture of trabecular bone. J Pathol **178:**100–105.
12. Odgaard A, Gundersen HJ 1993 Quantification of connectivity in cancellous bone, with special emphasis on 3-D reconstructions. Bone **14:**173–182.
13. Harrigan TP, Mann RW 1984 Characterization of microstructural anisotropy in orthotropic materials using a second rank tensor. J Mater Sci **19:**761–767.
14. Genant HK, Wu CY, vanKuijk C, Nevitt M 1994 Vertebral fracture assessment using a semi-quantitative technique. J Bone Miner Res **8:**1137–1148.
15. Gordon CL, Lang TF, Augat LP, Genant HK 1998 Image-based assessment of spinal trabecular bone structure from high-resolution CT images. Osteoporos Int **8:**317.
16. Link TM, Vieth V, Stehling C, Lotter A, Beer A, Newitt D, Majumdar S 2003 High-resolution MRI vs multislice spiral CT: Which technique depicts the trabecular bone structure best? Eur Radiol **13:**663.
17. Issever AS, Vieth V, Lotter A, Meier N, Laib A, Newitt D, Majumdar S, Link TM 2002 Local differences in the trabecular bone structure of the proximal femur depicted with high-spatial-resolution MR imaging and multisection CT. Acad Radiol **9:**1395.
18. Gordon CL, Webber CE, Christoforou N, Nahmias C 1997 In vivo assessment of trabecular bone structure at the distal radius from high-resolution magnetic resonance images. Med Phys **24:**585–593.
19. Majumdar S, Genant HK, Grampp S, Newitt DC, Truong V-H, Lin JC, Mathur A 1997 Correlation of trabecular bone structure with age, bone mineral density and osteoporotic status: In vivo studies in the distal radius using high resolution magnetic resonance imaging. J Bone Miner Res **12:**111–118.
20. Link TM, Majumdar S, Augat P, Lin JC, Newitt D, Lu Y, Lane NE, Genant HK 1998 In vivo high resolution MRI of the calcaneus: Differences in trabecular structure in osteoporosis patients. J Bone Miner Res **13:**1175–1182.
21. Majumdar S, Link TM, Augat P, Lin JC, Newitt D, Lane NE, Genant HK 1999 Trabecular bone architecture in the distal radius using magnetic resonance imaging in subjects with fractures of the proximal femur. Osteoporos Int **10:**231–239.
22. Majumdar S, Kothari M, Augat P, Newitt DC, Link TM, Lin JC, Lang T, Lu Y, Genant HK 1998 High-resolution magnetic resonance imaging: Three-dimensional trabecular bone architecture and biomechanical properties. Bone **22:**445–454.
23. Majumdar S, Newitt D, Mathur A, Osman D, Gies A, Chiu E, Lotz J, Kinney J, Genant H 1996 Magnetic resonance imaging of trabecular bone structure in the distal radius: Relationship with X-ray tomographic microscopy and biomechanics. Osteoporos Int **6:**376–385.
24. Wehrli F, Hwang S, Ma J, Song H, Ford J, Haddad J 1998 Cancellous bone volume and structure in the forearm: Noninvasive assessment with MR microimaging and image processing. Radiology **206:**347–357.
25. Lin J, Amling M, Newitt D, Selby K, Delling G, Genant H, Majumdar S 1996 Heterogeneity of trabecular bone structure in the calcaneus using high resolution magnetic resonance imaging (MRI). Osteoporos Int **8:**16–24.
26. Link T, Majumdar S, Lin J, Newitt D, Augat P, Ouyang X, Mathur A, Genant H 1998 A comparative study of trabecular bone properties in the spine and femur using high resolution MRI and CT. J Bone Miner Res **13:**122–132.
27. Kuehn B, Stampa B, Heller M, Glueer C 1997 In vivo assessment of trabecular bone structure of the human phalanges using high resolution magnetic resonance imaging. Osteoporos Int **7:**291.
28. Ross PD, Genant HK, Davis JW, Miller PD, Wasnich RD 1993 Predicting vertebral fracture incidence from prevalent fractures and bone density among non-black, osteoporotic women. Osteoporos Int **3:**120–126.
29. Njeh CF, Fuerst T, Hans D, Blake GM, Genant HK 1999 Radiation exposure in bone mineral density assessment. Appl Radiat Isot **50:**215.
30. Thornton FJ, Paulson EK, Yoshizumi TT, Frush DP, Nelson RC 2003 Single versus multi-detector row CT: Comparison of radiation doses and dose profiles. Acad Radiol **10:**379.
31. van Rietbergen B, Weinans H, Huiskes R, Odgaard A 1995 A new method to determine trabecular bone elastic properties and loading using micromechanical finite-element models. J Biomech **28:**69–81.
32. Ito M, Nishida A, Koga A, Ikeda S, Shiraishi A, Uetani M, Hayashi K, Nakamura T 2002 Contribution of trabecular and cortical components to the mechanical properties of bone and their regulating parameters. Bone **31:**351–358.

Address reprint requests to:
Masako Ito, MD
Division of Radiology
Nagasaki University Hospital
Nagasaki 852-8501, Japan
E-mail: masako@net.nagasaki-u.ac.jp

Received in original form February 16, 2005; revised form June 4, 2005; accepted June 16, 2005.

ELSEVIER

Bone 37 (2005) 497 – 503

BONE

www.elsevier.com/locate/bone

Ataxia telangiectasia mutated (*Atm*) knockout mice as a model of osteopenia due to impaired bone formation

Akinori Hishiya[a], Masako Ito[b], Hiroyuki Aburatani[c], Noboru Motoyama[d], Kyoji Ikeda[a], Ken Watanabe[a,*]

[a]*Department of Bone and Joint Disease, National Institute for Longevity Sciences (NILS), National Center for Geriatrics and Gerontology (NCGG), 36-3 Gengo, Morioka-cho, Obu, Aichi 474-8522, Japan*

[b]*Department of Radiology, Nagasaki University Hospital, Nagasaki, Japan*

[c]*Department of Cancer Systems Biology, Research Center for Advanced Science and Technology, The University of Tokyo, Tokyo, Japan*

[d]*Department of Geriatric Medicine, NCGG, Obu, Japan*

Received 19 December 2004; revised 11 April 2005; accepted 20 May 2005
Available online 18 July 2005

Abstract

ATM is a member of the PI-3 kinase protein family, encoded by the gene, *ATM*, responsible for ataxia telangiectasia (AT). AT is recognized as a genomic instability syndrome, sharing accelerated senescence symptoms in human and mouse. Here, we present evidence that the bone phenotype of *Atm* knockout (AtmKO) mice is similar to that observed in disuse and/or aging syndromes. A significant decrease in 3-dimensional bone volume fraction (BV/TV) of the fifth lumbar vertebra was observed in AtmKO mice by μCT, compared with heterozygous control mice at 10 weeks of age. Bone histomorphometry revealed that both BFR/BS and Oc.S/BS were significantly decreased in KO mice. To determine the cellular basis of this bone phenotype, we employed in vitro osteoclastogenesis and colony formation assays using bone marrow cells derived from KO and control mice. There was no difference in osteoclast formation in ex vivo cultures. CFU-F was markedly reduced in AtmKO-derived cultures compared with control mice, whereas differentiation of calvaria-derived osteoblasts did not differ between the genotypes. Furthermore, expression levels of IGF1R were significantly decreased, and p38 was aberrantly phosphorylated in marrow stromal cells from AtmKO mice. These results indicate that the pathogenesis of the osteopenic phenotype in AtmKO mice is similar to that of disuse and/or aging syndromes and is caused, at least in part, by a stem cell defect due to lack of IGF signaling.

Keywords: Premature aging syndrome; Animal models; Mesenchymal stem cells; Knockout

Introduction

Much progress has been achieved in our understanding of the pathogenesis of postmenopausal osteoporosis, characterized by accelerated bone resorption [1,2]. On the other hand, the pathophysiology of senile osteoporosis, caused mainly by declining bone-forming capacity, remains an enigma due to the lack of suitable animal models. Although aged (2 to 3 years old) animals are good candidates, natural aging is a complex phenomenon involving a plethora of factors and is difficult to dissect at the molecular level. Recently, genetically engineered mouse models for studying aging and age-related disorders have been developed [3]. Since they are caused by single gene mutations, they provide valuable tools for studying the pathogenesis of senile osteoporosis at the molecular level. For example, osteopenia with reduced bone formation and resorption has been reported in *klotho* (*kl/kl*) and mutant p53-expressing mice [4,5].

Ataxia telangiectasia (AT) is a human premature aging syndrome characterized by neurodegeneration, immune defects, tumor formation, hypersensitivity to ionizing radiation, and genomic instability [6]. The responsible gene, *ATM* (for AT mutated), is a large protein kinase that belongs

* Corresponding author. Fax: +81 562 44 6595.
E-mail address: kwatanab@nils.go.jp (K. Watanabe).

8756-3282/$ - see front matter © 2005 Elsevier Inc. All rights reserved.
doi:10.1016/j.bone.2005.05.012

to the PI-3 kinase family [10,11]. ATM functions in DNA damage checkpoint and oxidative stress responses, thereby playing a central role in the maintenance of genome stability. Mouse models for AT have been generated by knockout of the mouse Atm gene [7–9]. AtmKO mice exhibit radiosensitivity, genomic instability, growth retardation, and lymphoma, recapitulating main features of human AT [7–9]. The bone phenotype, however, has not been defined. Interestingly, mice deficient in Abl, a downstream protein kinase effector of ATM, exhibit an osteopenic phenotype with reduced bone formation [27]. We report here that AtmKO mice show osteopenia as early as 10 weeks of age, when growth retardation is not apparent. Histomorphometric and biochemical analyses revealed impaired bone formation, which may be caused by limited proliferative potential of osteogenic progenitors. Thus, AtmKO mice may provide a suitable model for studying senile osteoporosis.

Materials and methods

Mice

AtmKO mice (129/SvEv-*Atm*^{tm1Awb}) were obtained from Jackson Labs (Bar Harbor, Maine, USA). All generations were from matings of heterozygous parents. Genotyping was performed as described [9,12] with the exception of the primers used to detect the wild type allele. The primer sequences used for genotyping were as follows:

oIMR640, 5′-GCTGCCATACTTGATCAATG-3′
oIMR641, 5′-TCCGAATTTGCAGGAGTTG-3′.

The sequences used were recommended by Jackson Labs. All animal experiments were approved in advance by the Ethics Review Committee for Animal Experimentation of the National Institute for Longevity Sciences and the National Center for Geriatrics and Gerontology.

Bone morphological and histomorphometric analyses

Lumbar vertebrae and tibias were obtained from 6-, 10-, and 14-week-old female and male mice and subjected to morphological analyses ($n = 3 \sim 6$). Microcomputed tomography (μCT) and bone histomorphometry of the vertebrae and tibias, respectively, doubly labeled by calcein, were performed as described previously [13].

CFU assay

Colony forming unit (CFU) assays were conducted according to Jilka et al. [14]. Briefly, bone marrow cells were obtained from femurs or tibias and seeded at 1.5×10^6 (for CFU-F/CFU-ALP) or 2.5×10^6 (for CFU-Ob or CFU-Adip) cells/well in a 6-well plate. For CFU-F and CFU-Ob, the marrow cell cultures were maintained in phenol red-free αMEM containing 15% FCS and 1 mM Asc-2-P; one-half of the medium was replaced every 5 days. For CFU-Adip, the cultures were maintained in phenol red-free αMEM (Invitrogen, Carlsbad, California, USA) containing 15% FCS and MDI (0.5 mM methylisobutylxanthine, 1 μM dexamethasone, 1 μg/ml insulin) for 25–28 days. The cells were cultured for 10 days and then stained for ALP and counterstained with hematoxylin. Colonies of cells containing a minimum of 20 cells were designated as CFU-F, and those positive for ALP activity as CFU-ALP. For CFU-Ob, the cells were maintained for 25–28 days, fixed in 50% ethanol and 18% formaldehyde, and then stained using 2% Alizarin Red. The oil drops in the adipocytic cells were stained by Oil Red-O.

Osteoblastic cell cultures

Osteoblastic cells were isolated from calvarias of neonatal (P2–P3) AtmKO or wild-type mice following the protocol described by Jochum et al. [15] with minor modifications. For alkaline phosphatase (ALP) staining, osteoblastic cells were cultured in 24-well tissue culture plates. After reaching confluency, medium was supplemented with 60 μg/ml ascorbic acid and 10 nM dexamethasone and cultured for 7 more days. ALP staining was performed using a leukocyte alkaline phosphatase staining kit (SIGMA Diagnostics, St. Louis, USA). For ALP activity measurement, cells from the same conditions described above were washed with PBS and sonicated in RIPA buffer (50 mM Tris–HCl (pH 7.5) containing 150 mM NaCl, 1% NP-40, 0.5% sodium deoxycholate, and 0.1% sodium dodecyl sulfate). ALP activity in the lysate was measured using an ALP activity measurement kit (Wako Pure Chemical Industries, Osaka, Japan). The protein content was determined using BCA protein assay reagent (Pierce Chemical Co., Rockford, Illinois, USA).

M-CSF-dependent cell proliferation assay

Bone marrow cells were isolated from AtmKO or control mice, and the erythrocytes in the collected cells were depleted by standard ammonium-chloride lysis. To assess M-CSF-dependent proliferative response, cells (3×10^4) were cultured in flat-bottom 96-well plates for 2 days with various amounts of M-CSF (R&D Systems, Minneapolis, USA). Cultures were pulsed for 24 h with 1 μCi/well of [^{3}H]thymidine, harvested on glass-fiber filters, and the incorporated radioactivity was determined using a beta counter.

In vitro osteoclastogenesis assay

Bone marrow cells were isolated from AtmKO or control mice and incubated in tissue culture plates with αMEM containing 10% FCS. After 4 h in culture, nonadherent cells

were collected and counted. 5×10^5 cells were cultured for 3 days in 24-well tissue culture plates with 10 ng/ml M-CSF and for an additional 3 days in the presence of both 10 ng/ml M-CSF and 10 ng/ml RANKL (R&D Systems). Adherent cells were then fixed with an acetone–citrate–formalin solution (65:27:7) and stained for TRAP using a leukocyte acid phosphatase kit (SIGMA Diagnostics). The number of TRAP-positive multinucleated cells containing more than three nuclei was counted as osteoclasts.

Immunoblot analysis

Adherent cells from bone marrow of AtmKO or control mice were lysed in RIPA buffer containing 2 mM phenyl–methyl–sulfonyl fluoride, 10 mM sodium fluoride, 2 mM sodium vanadate, and proteinase inhibitor cocktail (Complete™, Roche Diagnostics, GmbH Mannheim, Germany). The cell lysates (15 μg each of protein) were subjected to SDS-PAGE, transferred, and then detected with antibodies using ECL-Plus (Amersham-Pharmacia). Anti-p38 (sc-535), anti-IGF1R (sc-713), and anti-c-Abl (sc-131) antibodies were purchased from Santa Cruz Biotechnology, California, USA. Anti-phosphorylated p38 (9211) and anti-tubulin (T5168) were obtained from Cell Signaling Technology (Beverly, Massachusetts, USA) and SIGMA, respectively.

IGF-dependent cell proliferation assay

Bone marrow cells were obtained as described above. The adherent cells were harvested and replated at a density of 5×10^4 cells/well in 96-well plates. After 24-h serum deprivation, the cultures were labeled with [^{3}H]thymidine with or without human recombinant IGF-I (10 ng/ml; Invitrogen). The incorporated [^{3}H] was measured as described.

Statistical analysis

Data are presented as mean ± SD. All data were analyzed by Student's *t* test. Statistical significance was considered at $P < 0.05$, unless otherwise indicated.

Results

Osteopenia due to impaired bone formation in AtmKO mice

To characterize the bone phenotype of Atm homozygous knockout mice with heterozygous littermates as controls, μCT scanning technique was employed. We analyzed 6-, 10-, and 14-week-old animals. At 6 weeks of age, there was no significant decrease in bone mass of AtmKO mice (data not shown). Since ovarian defect, which was possible to affect bone metabolism, was observed in female KO mice [7–9], we focused in the structural data from male animals. As shown in Figs. 1A and B, 3-dimensional bone volume (BV/TV) of the lumbar vertebrae was markedly decreased in AtmKO mice at 10 weeks of age. At this age, there is no significant difference in body weight between AtmKO and littermate control mice (24.8 ± 1.6 versus 21.5 ± 2.4 g). The trabecular number (Fig. 1C) and thickness (Fig. 1D) were also reduced in AtmKO mice compared to control. The difference between KO and control mice was more pronounced at age of 14 weeks, when some KO animals became cachexic.

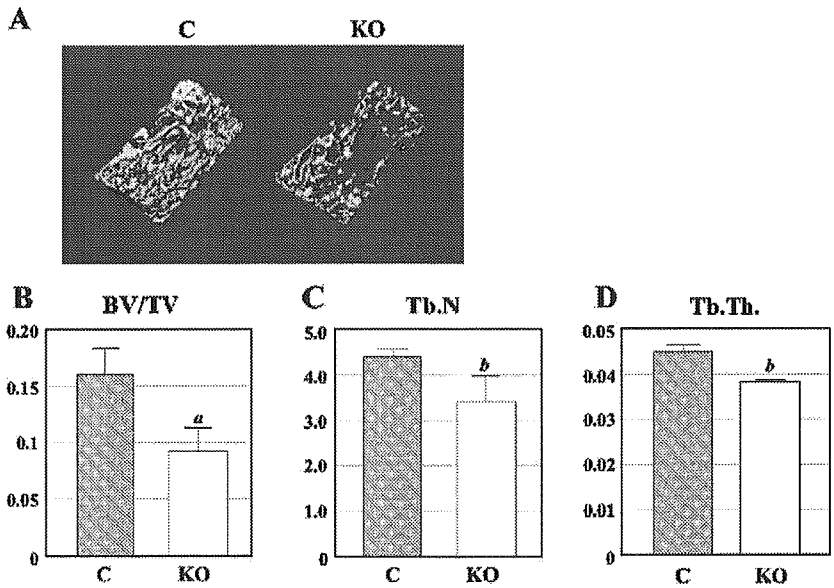

Fig. 1. Micro-CT analysis of lumber vertebrae of AtmKO mice. The fifth lumbar vertebra from heterozygous (C) and knockout (KO) mice were subjected to μCT analysis at 10 weeks of age. (A) Representative 3D images of trabecular architectures are shown. Note that the osteopenic phenotype was observed in knockout mice. (B) Trabecular bone volume fraction (BV/TV); (C) trabecular number (Tb.N); (D) trabecular thickness (Tb.Th.). The data were obtained in male mice. $^aP < 0.005$ and $^bP < 0.05$, significantly different from the respective heterozygous control group.

Bone histomorphometric analysis of the proximal tibia showed that bone formation rate (BFR/BS) and the osteoblast surface (Ob.S/BS) were significantly decreased in both female and male AtmKO mice (Fig. 2). The osteoclast surface (Oc.S/BS) was also reduced in the KO mice, suggesting that both bone formation and resorption were suppressed in AtmKO mice and that the observed osteopenic phenotype was caused mainly by impaired bone formation.

Cellular basis of impaired bone formation

To determine whether impaired bone formation was due to a cell autonomous defect, in vitro osteoblastogenesis assays were performed. The number of CFU-F (Fig. 3A), CFU-ALP (Fig. 3B), and CFU-OB (data not shown) were significantly reduced in the bone marrow of AtmKO mice. The decrease in CFU-F, which reflects the number and/or proliferative potential of mesenchymal progenitors, suggested that the defect was not specific to the osteoblastic lineage but involved other lineages as well. In fact, the number of CFU-adipocyte was also reduced (data not shown). We performed osteoblastogenesis assays in the presence of *N*-acetyl cysteine (NAC) to reduce oxidative stress, which often affects cell proliferation and induces senescence of primary cultured murine cells. As shown in Figs. 3A and B, supplementation with NAC increased the number of CFU-F and CFU-ALP in bone marrow cultures from control mice, but not in cultures from AtmKO mice. Notably, the ratio of CFU-ALP to CFU-F was not markedly altered between the genotypes, suggesting that differentiation, especially the ability to differentiate into osteoblasts, was not impaired in AtmKO mice.

To address the question whether the absence of Atm affected the differentiation process, osteoblasts were isolated from calvarias of homozygous and heterozygous knockout mice and cultured in vitro. As shown in Fig. 3C, calvaria-derived osteoblastic cells differentiated at comparable levels, suggesting that the differentiation potential of osteoblasts was not impaired in AtmKO mice. Together, with results from the CFU assays, these data collectively suggested that the impaired bone formation was not due to a defect in the differentiation program of osteoblasts per se but to the proliferative potential of mesenchymal progenitors.

As for the hematopoietic lineage, M-CSF-dependent proliferation of bone marrow cells from AtmKO mice did not differ from that of control mice (Fig. 4A). When osteoclastogenic potential was assessed in bone marrow cultures with M-CSF and RANKL, neither the number of TRAP-positive multinucleated cells formed (Fig. 4B) nor their morphology (Fig. 4C) differed between the genotypes.

Reduced IGF1 receptor with activation of p38 in Atm-deficient marrow stromal cells

To gain some insight into the molecular mechanism underlying the impaired proliferation of mesenchymal progenitors in AtmKO mice, the expression of molecules involved in ATM signaling was analyzed by immunoblotting. As shown in Fig. 5 (right lane), the level of phosphorylated p38MAPK (P-p38) was elevated in marrow stromal cells derived from AtmKO mice, while the total amount of p38 in the experimental and control cultures did not differ. By contrast, the expression of IGF-I receptor (IGF1R) was markedly reduced in AtmKO-derived marrow stromal cells compared with control cells (Fig. 5A). The level of Abl, a downstream effector molecule involved in the ATM pathway, did not differ between the genotypes. Next, we determined whether the IGF response was impaired in cells derived from AtmKO mice. As shown in Fig. 5B, control cells responded to IGF with increased proliferation, whereas the response to IGF was severely impaired in the stromal cells from AtmKO mice, suggesting that a decline in the expression level of IGF1R causes IGF-dependent proliferation in AtmKO mice.

Discussion

In the present study, we demonstrate that AtmKO mice show reduced bone formation due to a proliferative defect in

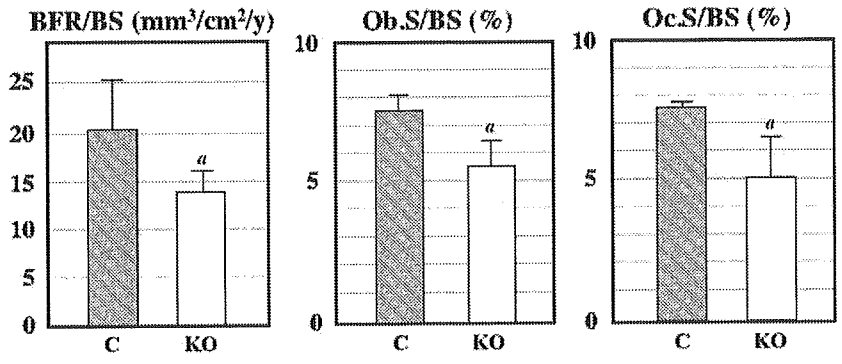

Fig. 2. Bone histomorphometric analysis of AtmKO mice. Decreases in bone formation rate (BFR/BS, left), osteoblast surface (Ob.S/BS, center), and osteoclast surface (Oc.S/BS, right) were measured from the proximal tibias of male AtmKO (KO) mice and compared with heterozygous (C) littermate controls. Data expressed are the means ± SD. $^{a}P < 0.05$, significantly different from the respective heterozygous control group.

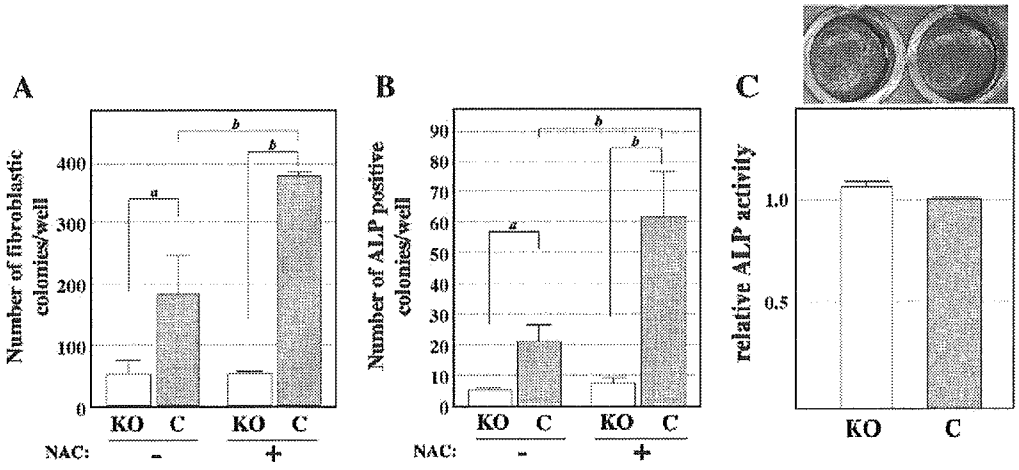

Fig. 3. Colony formation assay of bone marrow cells and calvarial osteoblast differentiation. (A) CFU-F in bone marrow cells derived from AtmKO (KO) or littermate wild-type or heterozygous control (C) mice (n = 3~5) are shown. (B) CFU-ALP. Note the significant reductions in both CFU-F and CFU-ALP ($P < 0.05$, KO versus control). N-acetyl cysteine (NAC, 10 mM) improved the numbers of CFU-F and CFU-ALP in control but not in cells from AtmKO mice. (C, upper panel) A representative photograph of the wells stained for ALP activity. Lower panel, relative ALP of calvarial cell cultures. No significant difference in morphology or ALP activity was observed between knockout (KO) and controls (C). Data represent the means ± SD. $^{a}P < 0.05$ and $^{b}P < 0.005$, significantly different from the respective control group. No significant difference was detected in the presence or absence of NAC in KO cells either in CFU-F or CFU-ALP assays.

mesenchymal progenitor cells, in addition to other age-related disorders observed in the human syndrome, AT, including neurodegeneration, immune defects, tumor formation, and genomic instability [7–9]. It has been suggested that, in mice as well as in humans, age-related decline in osteoblast number and function is caused by a decrease in number and proliferative potential of mesenchymal stem cells [16–19]. AtmKO mice recapitulate these cellular defects as early as 10 weeks of age. At this age, there are no signs of lymphoma or severe growth retardation in KO mice [7], suggesting that the bone phenotype is not caused by the secondary effects of those defects. The difference in bone mass between genotypes was more pronounced with age. The loss of bone mass associated with age may be accelerated by other abnormalities, such as growth retardation, lymphoma, immune defects, and cachexia. Importantly, we have shown in this study that the bone marrow cells exhibited a cell autonomous defect in proliferation. Therefore, it is suggested that the impairment in bone formation with a proliferative defect in bone marrow stem cells causes the osteopenic phenotype in AtmKO mice, although we cannot exclude the possibility that the defects such as T-lymphopenia and hypogonadism affected the bone phenotype of more aged mice. The microstructural alterations in the lumbar vertebrae of AtmKO mice are also similar to those observed in naturally aging C57BL/6J mice [20]. Thus, AtmKO mice may provide a suitable model to study the pathophysiology of senile osteoporosis without the necessity of raising them for 2 to 3 years.

Recently, Bonyadi et al. reported that Sca1 KO mice develop an age-dependent osteopenia [21]. Sca1 KO mice exhibit a decrease in the number of osteoprogenitors as well

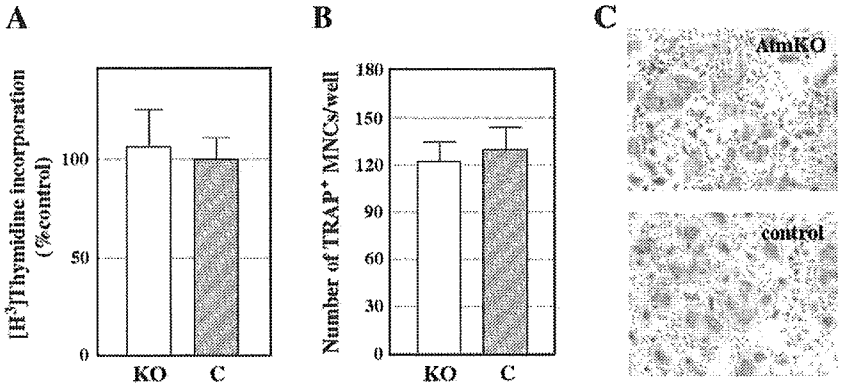

Fig. 4. M-CSF-dependent proliferation and in vitro osteoclastogenesis of bone marrow cells. (A) No obvious difference in M-CSF-dependent [^{3}H]thymidine incorporation into bone marrow cells was detected. (B) The number of multinucleated TRAP-positive cells derived from bone marrow cells in the presence of RANKL and M-CSF. No significant difference between the cells from AtmKO (KO) and littermate control (C) mice was observed. (C) TRAP staining of the in-vitro-generated multinucleated cells.

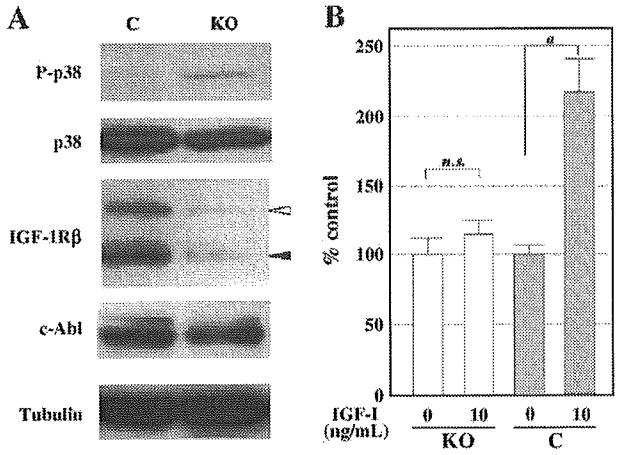

Fig. 5. Expression analysis of IGF-I receptor in bone marrow cells. (A) Total cell lysates of bone marrow stromal cells from wild-type (C, left lane) or Atm knockout (KO, right lane) were subjected to immunoblot analyses. Top panel (P-p38), activated (phosphorylated) p38. Second panel (p38), total p38 MAP kinase. The activated p38 is only detected in AtmKO. These two panels were from a membrane blot. Third panel (IGF-IRβ), probed with antibody against the insulin-like growth factor receptor β subunit. The upper (open arrowhead) and lower (closed arrowhead) bands correspond to unprocessed and processed β subunit protein, respectively. Fourth panel (c-Abl) shows expression level of c-Abl protein. The bottom panel, probed with anti-tubulin antibody to control for protein loading in the last three panels (IGF-IRβ, c-Abl). (B) IGF-I response. Bone marrow stromal cells from Atm knockout (KO) or wild-type (C) were cultured with or without IGF-I. Incorporated thymidine was measured and displayed as fold change (%) compared to culture without IGF for each genotype. $^{a}P < 0.005$; n.s., not significant.

as CFU-F and have a non-cell autonomous defect in osteoclasts [21]. Although defects of osteoblasts and osteoclasts are similarly observed in AtmKO mice, the expression of Sca1 mRNA was not altered in AtmKO mice (data not shown). Additionally, the onset of the bone phenotype in Sca1 KO (~12 months of age) was very late, compared with that of AtmKO mice (~10 weeks). Thus, the impact of ATM deficiency on bone formation was more severe than that of Sca1 deficiency.

It has been reported that AtmKO mice showed reduced numbers of leukocytes in the circulation as well as bone marrow [7–9,22]. Although osteoclast surface was reduced in the bone of AtmKO mice, osteoclastogenic potential as well as M-CSF-dependent cell proliferation in vitro was normal, pointing to the involvement of impaired ability of the marrow environment to support proliferation/differentiation of osteoclast progenitors rather than cell autonomous dysfunction in the hematopoietic lineage. Concerning the osteoblastic lineage of AtmKO mice, the defect lies mainly in CFU-F, while the differentiation of osteoblasts was rather normal. Thus, it is tempting to speculate that multi-potent stem or progenitor cells are more sensitive to Atm deficiency than are differentiated cells. As we did not find any difference in the expression of Jagged-1 (data not shown), one of the key molecules that function in the bone marrow niche [23], the molecular defect in niche function of AtmKO mice remains to be clarified.

Chk2 is a checkpoint kinase that functions downstream of ATM and phosphorylates p53 to stabilize it [11,24]. Soft X-ray analysis of bones from Chk2 KO mice [25] revealed no alteration in bone density (AH et al., unpublished observation). It has been reported that the bones of mice lacking p53, the target of ATM and Chk2 kinases, were normal, although they were resistant to bone loss in response to unloading [26]. Thus, it is unlikely that the Chk2 pathway is involved in the impaired bone formation in AtmKO mice.

It has been reported that mice lacking Abl, another downstream kinase of ATM, exhibit an osteopenic phenotype due to reduced bone formation, which is caused mainly by a defect in osteoblast differentiation [27]. In AtmKO mice, by contrast, osteoblastic differentiation is normal. Li et al. have recently demonstrated distinct roles for ATM and Abl in the oxidative stress response and that ATM and Abl differentially regulate osteoblast expression of PKCδ [28]. We demonstrated that the improved colony formation following supplementation with NAC was diminished in AtmKO-derived cultures. Thus, the possibility exists that irreversible damage by oxidative stress had already altered the proliferative potential of AtmKO-derived progenitor cells or that an additional molecular defect(s), other than the oxidative stress response, is involved.

IGF plays important roles in bone growth and metabolism [29–31]. This has been supported by genetic approaches in mice [32–35]. *ATM* deficiency downregulates the transcription of the *IGF1R* gene [36], and we found, in fact, that the expression of IGF1R, as well as the responsiveness to IGF, was decreased in marrow stromal cells of AtmKO mice. These results indicate that defective IGF signaling may be involved in the impaired bone formation observed in AtmKO mice. In addition, since serum deprivation induces oxidative stress, due mainly to loss of IGF [37], the connection between IGF activity and oxidative stress may be an interesting relationship warranting further investigation.

In conclusion, we demonstrate that AtmKO mice present an osteopenic phenotype as early as 10 weeks, apparently due to decreased bone-marrow-derived mesenchymal progenitors. This decline in mesenchymal progenitors may be the result of decreased expression of IGF1R, an important regulator of proliferation. The AtmKO mouse model may be a useful tool for further studies of senile osteoporosis.

Acknowledgments

The authors thank Drs. Yoshiko Masuda and Aya Sasaki for technical assistance in bone analyses; Miho Kamiya, Makiko Matsuura, and Kumi Tsutsumi for in vitro experiments and genotyping; Dr. Kazuhito Naka for advise in analyses of protein expression; and Dr. Akira Matsuura for critical reading of the manuscript. This study was supported in part by a grant from the Program for Promotion of Fundamental Studies in Health Sciences of the Organiza-

tion for Pharmaceutical Safety and Research of Japan and by a Research Grant for Longevity Sciences from the Ministry of Health, Labor and Welfare.

References

[1] Bilezikian JP, Raisz LG, Rodan GA, editors. Principles of bone biology. San Diego, CA: Academic Press; 2002.
[2] Favus MJ, editor. Primer on the metabolic bone diseases and disorders of mineral metabolism. American Society for Bone and Mineral Research; 2003.
[3] Hasty P, Vijg J. Accelerating aging by mouse reverse genetics: a rational approach to understanding longevity. Aging Cell 2004;3:55–65.
[4] Tyner SD, Venkatachalam S, Choi J, Jones S, Ghebranious N, Igelmann H, et al. p53 mutant mice that display early ageing-associated phenotypes. Nature 2002;415:45–53.
[5] Kuro-o M, Matsumura Y, Aizawa H, Kawaguchi H, Suga T, Utsugi T, et al. Mutation of the mouse klotho gene leads to a syndrome resembling ageing. Nature 1997;390:45–51.
[6] Lavin MF, Shiloh Y. The genetic defect in ataxia-telangiectasia. Annu Rev Immunol 1997;15:177–202.
[7] Barlow C, Hirotsune S, Paylor R, Liyanage M, Eckhaus M, Collins F, et al. Atm-deficient mice: a paradigm of ataxia telangiectasia. Cell 1996;86:159–71.
[8] Elson A, Wang Y, Daugherty CJ, Morton CC, Zhou F, Campos-Torres J, et al. Pleiotropic defects in ataxia-telangiectasia protein-deficient mice. Proc Natl Acad Sci U S A 1996;93:13084–9.
[9] Xu Y, Ashley T, Brainerd EE, Bronson RT, Meyn MS, Baltimore D. Targeted disruption of ATM leads to growth retardation, chromosomal fragmentation during meiosis, immune defects, and thymic lymphoma. Genes Dev 1996;10:2411–22.
[10] Rotman G, Shiloh Y. ATM: from gene to function. Hum Mol Genet 1998;7:1555–63.
[11] Shiloh Y. ATM and related protein kinases: safeguarding genome integrity. Nat Rev Cancer 2003;3:155–68.
[12] Liao MJ, Van Dyke T. Critical role for Atm in suppressing V(D)J recombination-driven thymic lymphoma. Genes Dev 1999;13:1246–50.
[13] Shibata T, Shira-Ishi A, Sato T, Masaki T, Masuda A, Hishiya A, et al. Vitamin D hormone inhibits osteoclastogenesis in vivo by decreasing the pool of osteoclast precursors in bone marrow. J Bone Miner Res 2002;17:622–9.
[14] Jilka RL, Weinstein RS, Takahashi K, Parfitt AM, Manolagas SC. Linkage of decreased bone mass with impaired osteoblastogenesis in a murine model of accelerated senescence. J Clin Invest 1996;97:1732–40.
[15] Jochum W, David JP, Elliott C, Wutz A, Plenk Jr H, Matsuo K, et al. Increased bone formation and osteosclerosis in mice overexpressing the transcription factor Fra-1. Nat Med 2000;6:980–4.
[16] Tsuji T, Hughes FJ, McCulloch CA, Melcher AH. Effects of donor age on osteogenic cells of rat bone marrow in vitro. Mech Ageing Dev 1990;51:121–32.
[17] Kahn A, Gibbons R, Perkins S, Gazit D. Age-related bone loss. A hypothesis and initial assessment in mice. Clin Orthop 1995:69–75.
[18] Bergman RJ, Gazit D, Kahn AJ, Gruber H, McDougall S, Hahn TJ. Age-related changes in osteogenic stem cells in mice. J Bone Miner Res 1996;11:568–77.
[19] D'Ippolito G, Schiller PC, Ricordi C, Roos BA, Howard GA. Age-related osteogenic potential of mesenchymal stromal stem cells from human vertebral bone marrow. J Bone Miner Res 1999;14:1115–22.
[20] Halloran BP, Ferguson VL, Simske SJ, Burghardt A, Venton LL, Majumdar S. Changes in bone structure and mass with advancing age in the male C57BL/6J mouse. J Bone Miner Res 2002;17:1044–50.
[21] Bonyadi M, Waldman SD, Liu D, Aubin JE, Grynpas MD, Stanford WL. Mesenchymal progenitor self-renewal deficiency leads to age-dependent osteoporosis in Sca-1/Ly-6A null mice. Proc Natl Acad Sci U S A 2003;100:5840–5.
[22] Peter Y, Rotman G, Lotem J, Elson A, Shiloh Y, Groner Y. Elevated Cu/Zn-SOD exacerbates radiation sensitivity and hematopoietic abnormalities of Atm-deficient mice. EMBO J 2001;20:1538–46.
[23] Calvi LM, Adams GB, Weibrecht KW, Weber JM, Olson DP, Knight MC, et al. Osteoblastic cells regulate the haematopoietic stem cell niche. Nature 2003;425:841–6.
[24] Chaturvedi P, Eng WK, Zhu Y, Mattern MR, Mishra R, Hurle MR, et al. Mammalian Chk2 is a downstream effector of the ATM-dependent DNA damage checkpoint pathway. Oncogene 1999;18:4047–54.
[25] Takai H, Naka K, Okada Y, Watanabe M, Harada N, Saito S, et al. Chk2-deficient mice exhibit radioresistance and defective p53-mediated transcription. EMBO J 2002;21:5195–205.
[26] Sakai A, Sakata T, Tanaka S, Okazaki R, Kunugita N, Norimura T, et al. Disruption of the p53 gene results in preserved trabecular bone mass and bone formation after mechanical unloading. J Bone Miner Res 2002;17:119–27.
[27] Li B, Boast S, de los Santos K, Schieren I, Quiroz M, Teitelbaum SL, et al. Mice deficient in Abl are osteoporotic and have defects in osteoblast maturation. Nat Genet 2000;24:304–8.
[28] Li B, Wang X, Rasheed N, Hu Y, Boast S, Ishii T, et al. Distinct roles of c-Abl and Atm in oxidative stress response are mediated by protein kinase C delta. Genes Dev 2004;18:1824–37.
[29] Baylink DJ, Finkelman RD, Mohan S. Growth factors to stimulate bone formation. J Bone Miner Res 1993;8(Suppl. 2):S565–72.
[30] Delany AM, Pash JM, Canalis E. Cellular and clinical perspectives on skeletal insulin-like growth factor I. J Cell Biochem 1994;55:328–33.
[31] Hayden JM, Mohan S, Baylink DJ. The insulin-like growth factor system and the coupling of formation to resorption. Bone 1995;17: 93S–8S.
[32] Zhang M, Xuan S, Bouxsein ML, von Stechow D, Akeno N, Faugere MC, et al. Osteoblast-specific knockout of the insulin-like growth factor (IGF) receptor gene reveals an essential role of IGF signaling in bone matrix mineralization. J Biol Chem 2002;277: 44005–12.
[33] Devlin RD, Du Z, Buccilli V, Jorgetti V, Canalis E. Transgenic mice overexpressing insulin-like growth factor binding protein-5 display transiently decreased osteoblastic function and osteopenia. Endocrinology 2002;143:3955–62.
[34] Bikle DD, Sakata T, Leary C, Elalieh H, Ginzinger D, Rosen CJ, et al. Insulin-like growth factor I is required for the anabolic actions of parathyroid hormone on mouse bone. J Bone Miner Res 2002;17: 1570–8.
[35] Woitge HW, Kream BE. Calvariae from fetal mice with a disrupted Igf1 gene have reduced rates of collagen synthesis but maintain responsiveness to glucocorticoids. J Bone Miner Res 2000;15:1956–64.
[36] Peretz S, Jensen R, Baserga R, Glazer PM. ATM-dependent expression of the insulin-like growth factor-I receptor in a pathway regulating radiation response. Proc Natl Acad Sci U S A 2001;98:1676–81.
[37] Busiguina S, Fernandez AM, Barrios V, Clark R, Tolbert DL, Berciano J, et al. Neurodegeneration is associated to changes in serum insulin-like growth factors. Neurobiol Dis 2000;7:657–65.

Journal of Receptors and Signal Transduction, 25:199–216, 2005

ISSN: 1079-9893 print / 1532-4281 online
DOI: 10.1080/10799890500240781

Taylor & Francis
Taylor & Francis Group

A RANKL-Inducible Gene *Znf216* in Osteoclast Differentiation

Akinori Hishiya, Kyoji Ikeda, and Ken Watanabe

Department of Bone and Joint Disease, National Center for Geriatrics and Gerontology (NCGG), Obu, Aichi, Japan

Osteoclasts possess catabolic activity in mineralized tissues and are involved in bone remodeling coordinating with osteoblasts. Although the pathway using receptor and activator of NF-κB (RANK) and its ligand, RANKL, is known to be essential for osteoclast differentiation, their precise mechanisms are not fully understood. Using DNA microarray technology, we searched for genes that were up-regulated after RANKL stimulation in the macrophage cell line, RAW264.7 cells. A gene, *Znf216,* which encodes a zinc-finger protein, was detected among those genes up-regulated after RANKL stimulation. Expression of *Znf216* was also induced by other cytokines such as TNFα and IL-1β. Although ectopic expression of full-length ZNF216 abrogated osteoclast differentiation, its truncated forms accelerated it. No significant inhibitory effect on the NF-κB pathway was observed, however. These results suggest that ZNF216 is a potent inhibitory factor for osteoclast differentiation and that the mechanism is unlikely due to direct attenuation of the NF-κB pathway.

Key Words: RANKL; cDNA microarray; ZNF216

INTRODUCTION

Osteoclasts are multinucleated giant cells derived from the hematopoietic lineage (1). A number of extracellular factors expressed at distinct stages are involved in osteoclast differentiation (2,3). For example, studies in the *op / op* mice, which are severely osteopetorotic due to the absence of osteoclasts, revealed that M-CSF plays a critical role in osteoclast differentiation (4). Proinflammatory cytokines, such as TNFα and IL-1β also accelerate osteoclast differentiation (5,6).

Address correspondence to Ken Watanabe, PhD, Department of Bone and Joint Disease, National Center for Geriatrics and Gerontology (NCGG), 36-3 Gengo, Morioka-cho, Obu, Aichi 474-8522, Japan. Tel: +81-562-46-2311; Fax: +81-562-44-6595; E-mail: kwatanab@nils.go.jp

Among the cytokines, the essential key regulator for osteoclast differentiation is a TNF family cytokine, RANKL (7,8). Mice lacking RANKL or its receptor, RANK, display severe osteopetorosis with a complete absence of osteoclasts, suggesting that the RANKL-RANK pathway is indispensable for osteoclast differentiation (9,10). This pathway promotes not only osteoclast differentiation but also activation (7) and survival (11).

The intracellular signaling events that mediate osteoclast differentiation have been studied by using genetic approaches. Double knockout mice of the p50 and p52 subunits of the transcription factor, NF-κB, display osteopetrosis as seen in RANKL null mice (12). NF-κB functions downstream of the RANKL-RANK pathway and presumably activates genes necessary for osteoclast differentiation. Knockout mice for *fos*, a member of the AP-1 family, also exhibit osteopetorosis (13). c-Fos is thought to be activated by the RANKL-RANK pathway, although the precise mechanism of action remains unknown (14). In addition, src kinase is activated by the RANKL-RANK pathway, and even though src-deficient mice display normal number of osteoclasts, their resorption activity is impaired (15,16). Src is known to be localized to ruffled border membranes, where bone resorption takes place (17). Collectively, these results show that a number of signaling molecules are involved in RANKL-induced osteoclast differentiation and function, although the downstream and the regulatory mechanism have not been fully elucidated.

In the present study, we used cDNA microarray technology to elucidate changes in gene expression during osteoclast differentiation. Among the genes up-regulated, *znf216* is also activated by proinflammatory cytokines, such as TNFα and IL-1β. Furthermore, overexpression of ZNF216 strongly inhibits RANKL-induced osteoclast differentiation. Thus, novel negative regulation may exist for osteoclast differentiation downstream of RANKL stimulation.

MATERIALS AND METHODS

Antibodies and Reagents

Anti-ZNF216 antibody was raised against a synthesized peptide corresponding to the C-terminal sequence of mouse ZNF216 (amino acids 200–213). Mouse monoclonal antibodies for FLAG (M2 and M5) and tubulin (B-5-1-2) were purchased from Sigma (St. Louis, MO, USA). Antibodies against IκBα (C-21), p50 (C-19), p52 (C-5), and p65 (A) were obtained from Santa Cruz Biotechnology (Santa Cruz, CA, USA). RANKL, TNFα, and IL-1β were purchased from R&D Systems (Minneapolis, MN, USA). Lipopolysaccharide (LPS) and TPA (12-*O*-tetradecanoylphorbol-13-acetate) were purchased from Sigma and IFNγ from Genzyme (Cambridge, MA, USA).

Cell Culture Transfection

RAW264.7 mouse monocyte/macrophage cells were maintained in α-modified Eagle's medium (αMEM) containing 10% heat-inactivated fetal bovine serum (FBS) supplemented with penicillin, streptomycin, and L-glutamate. For in vitro osteoclastogenesis, RAW264.7 cells were plated at a density of $1.3 \times 10^4/cm^2$ and incubated overnight. Recombinant mouse RANKL was then added to a final concentration of 10 ng/mL. To detect tartrate-resistant acid phosphatase (TRAP) activity, a hallmark of osteoclasts, cells were fixed with an acetone-citrate-formalin solution (65:27:7) and stained by using a leukocyte acid phosphatase kit (Sigma Diagnostics). For isolation of RNA, RAW264.7 cells were stimulated with TNFα (10 ng/mL), IL-1β (10 ng/mL), LPS (10 μg/mL), TPA (1 mM), or IFNγ (100 U/mL), and harvested at the indicated time points. RANK293 cells, which constitutively express RANK, were kindly provided by Drs. Naoki Sakurai (Tanabe Seiyaku Co., Ltd., Osaka, Japan) and Kunihiro Matsumoto (Nagoya University, Japan) (18). HEK293 and RANK293 cells were cultured at 37°C in Dulbecco's modified Eagle's medium (DMEM) containing 10% heat-inactivated FBS supplemented with penicillin and streptomycin. FuGENE6 (Roche Diagnostics, Mannheim, Germany) was used for transfection. RAW264.7 cells stably expressing full-length or truncated forms of ZNF216 were established by infection using Pantropic Retroviral Expression System (Clontech Laboratories, Palo Alto, CA, USA) and maintained in media containing puromycin.

Isolation of RNA and cDNA Microarray

Total RNA was isolated from RAW264.7 cells at 24, 48, and 72 hr after addition of RANKL. Untreated RAW264.7 cells were used as $t = 0$ hr control. Total RNA was purified by using TRIZOL Reagent (Invitrogen, Carlsbad, CA, USA), according to the manufacturer's instructions. Purification of mRNA was performed by using Micro-Fast Track 2.0 (Invitrogen). Purified mRNA was subsequently used for cDNA microarray analyses (Mouse GEM-I, Incyte Genomics, Palo Alto, CA, USA).

Plasmid Construction

Full-length ZNF216 cDNA was amplified by reverse transcription-coupled PCR (RT-PCR) and subcloned into pBabe-puro retrovirus vector or pEF4 /Myc-HisA (Invitrogen) with a FLAG epitope tag at the N-terminus to generate pF-ZNF216. Zinc finger-deleted mutants, ZNF216ΔN (amino acids 36–213) and ZNF216ΔC (amino acids 1–153), were also generated by PCR and subcloned into the vectors. All cDNAs and constructs amplified by PCR were fully sequenced (ABI PRISM^{TM} 3100 Genetic Analyzer, Applied Biosystems, Foster City, CA, USA).

Northern Blot Analysis

Total RNA was denatured by glyoxal/dimethylsulfoxide and electrophoresed on a 0.9% agarose gel and transferred to a nylon membrane (Amersham Biosciences, Little Chalfont, Buckinghamshire, England). To detect the indicated mRNA, cDNA was labeled with ^{32}P with use of DNA labeling beads (Amersham Biosciences).

Immunoblot Analysis

For chasing IκBα degradation, cells were lyzed in lysis buffer (50 mM Tris-HCl, 150 mM NaCl, 1.0% NP-40, 0.5% sodium deoxycholate, 0.1% SDS, pH7.5). Aliquots of lysates were separated by SDS-PAGE and immunoblotted. Visualization was done by ECL Plus reagents (Amersham Biosciences). For nuclear translocation of NF-κB, cells were lyzed and suspended in hypotonic buffer (50 mM HEPES-KOH, 10 mM KCl, 0.1 mM EDTA, 0.1% NP-40, and protease inhibitor cocktail, pH7.8). Nuclei were pelleted by centrifugation, and the cytosolic fraction was removed. The nuclei were resuspended in extraction buffer (50 mM HEPES-KOH, 420 mM KCl, 0.1 mM EDTA, 5 mM $MgCl_2$, 2% glycerol, and protease inhibitor cocktail, pH7.8), and rotated for 30 min in 4°C. The samples were centrifuged to remove debris. Protein content was measured by using BCA protein assay reagent (PIERCE, Rockford, IL, USA).

Electrophoretic Mobility Shift Assay (EMSA)

EMSA was performed as described by Yousef with minor modification (19). Briefly, RANK293 cells treated with RANKL were washed with ice-cold PBS, and then nuclear extracts were prepared as described above. Ten micrograms of the nuclear extract were incubated with an end-labeled double-stranded oligonucleotide probe containing the sequence 5′-AAA CAG GGG GCT TTC CCT CCT C-3′ derived from the κB3 site of the TNF promoter. The reaction was performed in a total of 20 μL of binding buffer (10 mM HEPES-KOH, 50 mM KCl, 1 mM EDTA, 5 mM $MgCl_2$, 3 μg poly dI-dC, and 10% glycerol, pH7.8) for 30 min at room temperature. Samples were then fractionated in a 4% polyacrylamide gel and visualized by exposing the dried gel to film.

Reporter Gene Assay

HEK293 cells were seeded onto 24-well culture plates and transfected with 10 ng pNF-κB-Luc plasmid (Stratagene, La Jolla, CA, USA), and 5 or 25 ng of ZNF216 full-length or mutant-expressing plasmid. Twenty-four hours after transfection, cells were incubated with low-serum-containing medium (0.5% FBS) for 24 hr, and then TNFα (100 ng/mL) was added. 24 hr after the addition of the cytokine, cells were harvested. For AP-1 reporter gene assays, 100 ng

pAP1-Luc plasmid (Stratagene) was transfected with or without 250 ng ZNF216 full-length-expressing plasmid. AP-1 activation was conducted by using 10 ng pFC-MEKK positive control plasmid (Stratagene). In all transfection experiments, 10 ng Renilla luciferase expression vector, phRG-TK (Promega, Madison, WI, USA), was used as an internal control and for normalization of transfection efficiency. The luciferase activity was measured by using the Dual-Luciferase Reporter Assay System (Promega).

RESULTS

Gene Expression Profile of RANKL-Induced Osteoclast Differentiation

RANKL-treated RAW264.7 cells were efficiently differentiated to osteoclast-like cells (OCLs) within 4 days, as evidenced by multiple nuclei and expression of the osteoclast marker, TRAP (not shown). Isolated RNAs were applied to a cDNA microarray to determine the relative expression levels of about 10,000 mouse genes in response to RANKL stimulation. Analyses revealed that 208 genes were up-regulated, and 515 genes were down-regulated, more than 1.7-fold for at least one time point over a 72-h time-course. A select list of genes differentially expressed are listed in Tables 1 and 2. Genes characteristic for osteoclasts, such as vacuolar ATPases, carbonic anhydrases, and matrix metalloproteinase 9, were up-regulated (Table 1), whereas macrophage-related genes, such as lysozyme and macrophage expressed gene 1, were prominently down-regulated (Table 2). These data collectively suggest that the profiling represents the transition of macrophages into osteoclasts. Among the up-regulated genes, those encoding transcription factors were evident, including c-myc and NFATc1. It was previously reported that c-myc was strongly induced by RANKL and that a dominant negative form of c-myc suppressed osteoclast differentiation (20), suggesting c-myc as a transcription factor involved in the promotion of osteoclastogenesis under the RANKL-RANK pathway. NFATc1 was also shown to be a downstream gene of c-fos, which is known to be activated by RANKL, and osteoclastogenesis of precursor cells of c-Fos$^{-/-}$ mice was rescued by forced expression of the active form of NFATc1 (21).

Another interesting finding was the down-regulation of interferon-induced genes. Takayanagi et al. (22) showed that IFNγ was a potent inhibitor of osteoclastogenesis. Treatment of RAW264.7 cells with IFNγ resulted in rapid degradation of the adaptor protein, TRAF6, via the ubiquitin-proteasome system. The expression of STAT1, which is activated by IFNγ, was also suppressed by RANKL. These results suggest that interferon itself or a pivotal transcription factor for interferon signaling, such as STAT1, is down-regulated during RANKL-induced osteoclastogenesis.

Table 1: Genes up-regulated during RANKL-induced osteoclast differentiation. Fold increase compared to $t = 0$ at the indicated time points is shown.

Gene description	UniGene ID	Fold		
		24 hr	48 hr	72 hr
Bone resorption				
Vocuolar ATPase catalytic subunit A	Mm.29771		1.9	2.4
ATPase-like vacuolar proton channel	Mm.30155	1.7	2.1	2.5
Carbonic anhydrase 1	Mm.3471		1.9	
Carbonic anhydrase 2	Mm.1186	1.5	1.7	2.3
Matrix metalloproteinase 9	Mm.4406		2.0	1.5
Signaling				
TRAF1	Mm.12898		2.5	1.6
TRAF5	Mm.196445		2.0	
skp2	Mm.35584		3.0	1.4
Transcription				
NFATc1	Mm.329560		3.2	1.8
Myc	Mm.2444	3.1	2.1	1.5
Fra2	Mm.24684	3.7	2.7	2.6
forkhead box G1	Mm.4704		3.2	
NF-kB2	Mm.102365	2.3		
Gbx2	Mm.204730		1.9	
Hoxa2	Mm.131		2.6	
Cytokine				
IL-15	Mm.4392		2.0	1.4
PDGF	Mm.2675		2.4	
Small inducible cytokine A9	Mm.2271		2.7	2.1
Other				
Aldose reductase	Mm.451			2.7
Butyrate response factor 1	Mm.18571	1.9	1.7	1.7
DNA polymerase epsilon, subunit 2	Mm.9199		3.0	
GABA-A transporter 2	Mm.22562	1.3	1.7	2.0
H1-0 histone	Mm.24350		2.5	
gly96	Mm.25613		2.2	2.2
slug	Mm.4272		2.7	
ZNF216	Mm.292405		3.0	2.2

Expression of ZNF216 in RANKL-Induced Osteoclast Differentiation

Microarray results also indicated that the gene encoding ZNF216 was potently induced by RANKL. Although *znf216* was first identified as a candidate gene that might be involved in autosomal recessive nonsyndromic hearing loss (ARNSHL), neither disease-causing mutations nor abnormal expression of the gene was found (23). To verify the cDNA microarray results, we carried out Northern blot analysis. The entire coding region of ZNF216 was used as a probe recognizing 2.4-kb and 1.5-kb mRNA species, derived from alternative splicing and polyadenylation. Both species were up-regulated by RANKL as early as 1 hr and peaked 48 hr after addition of the cytokine (Fig. 1A). As shown in Figure 1B, induction of the protein was confirmed by immunoblotting using anti-ZNF216 antibody. An approximately 32-kDa protein was recognized and increased dramatically after RANKL stimulation. Although the expression

Table 2: Genes down-regulated during RANKL-induced osteoclast differentiation. Fold decrease compared to $t = 0$ at the indicated time points is shown.

Gene description	UniGene ID	Fold		
		24 hr	48 hr	72 hr
Macrophage-related				
Lysozyme	Mm.45436		−29.6	−11.4
Macrophage expressed gene 1	Mm.3999	−4.6	−3.3	−3.9
β2 microglobuline	Mm.163		−2.4	−2.7
Fc receptor IgE	Mm.22673		−2.5	−1.8
Fc receptor IgG high affinity I	Mm.150		−3.4	−2.8
Histocompatibility 2 L region	Mm.260691		−1.9	−1.4
Histocompatibility 2 Q region	Mm.34421		2.4	−2.1
Histocompatibility 2 T region	Mm.221296		−2.2	−2.3
Signaling				
Adenylate cyclase 7	Mm.288206	−1.3	−2.0	−1.6
Adenylate cyclase-associated CAP protein	Mm.8687		−3.5	−3.0
Calmodulin 2	Mm.18041		−1.9	−1.5
STAT 1	Mm.8249		−2.2	−2.3
JAK2	Mm.809	−2.2		
Ribosomal protein S6 kinase, polypeptide 4	Mm.20914		−2.1	
MAPK14	Mm.4437		−1.7	−2.2
MAPKKK1	Mm.15918		−2.0	−1.5
AMP-dependent protein kinase	Mm.16766	−1.7	−1.9	−2.1
fyn proto-oncogene	Mm.4848		−1.6	−2.0
Cell cycle and differentiation				
Id2	Mm.34871		−3.8	−2.2
Id3	Mm.110		−2.0	−2.5
cyclin D1	Mm.273049		−1.6	−2.3
cdk2	Mm.118			−2.0
p21	Mm.34446	−1.3	−1.7	−2.5
Matrix protein and secreted-protein related				
ADAM15	Mm.19830		−1.9	−2.0
ADAM17	Mm.355306		−2.2	−1.8
IGF-1	Mm.268521	−3.6	−2.2	
IGF-1 binding protein 4	Mm.233799		−2.2	−2.3
Osteopontin	Mm.288474	−2.6	−4.0	−1.6
Interferon induced gene				
Interferon activated gene 203	Mm.261270	−2.2	−2.1	−2.0
Interferon activated gene 204	Mm.212870		−2.5	
Interferon dependent positive acting transcriptio factor 3	Mm.2032		−1.8	−2.0
Interferon γ inducible protein	Mm.24769		−2.0	−1.5
Interferon regulatory factor 5	Mm.6479		−2.0	−2.0
Interferon regulatory factor 7	Mm.3233		−3.8	−3.0
Interferon induced protein with tetratricopeptide repeat 3	Mm.271850		−1.5	−2.4
2′-5′ oligoadenylate synthetase 1A	Mm.14301	−1.5	−3.6	−1.4
Lysosomal protein				
Cathepsin D	Mm.231395		−3.0	−2.3
Cathepsin L	Mm.930	−1.5	−4.8	−5.9
Cathepsin S	Mm.3619	−2.4	−2.6	−2.1
Lysosomal membrane glycoprotein 2	Mm.486		−2.4	−1.7
Other				
Annexin A2	Mm.238343		−1.6	−2.1
Caspase 1	Mm.1051	−1.7	−1.5	−2.6
Coronin	Mm.27317	−1.7	−2.4	−2.1
Amyloid beta precursor protein	Mm.277585	−1.5	−1.8	−2.1
Glycoprotein 49A	Mm.196617			−2.6
Glycoprotein 49B	Mm.34408	−3.2	−4.0	−2.2
LIM only 2	Mm.29266		−2.9	−3.2
Schlafen 4	Mm.38192	−1.6	−5.1	−2.4
Cell surface glycoprotein EMR 1 precursor	Mm.258979	−2.5	−3.1	−3.5
Peroxiredoxin 4	Mm.247542			−1.9
Peroxiredoxin 5	Mm.279782			−2.1
Pleckstrin	Mm.98232		−6.6	−2.3

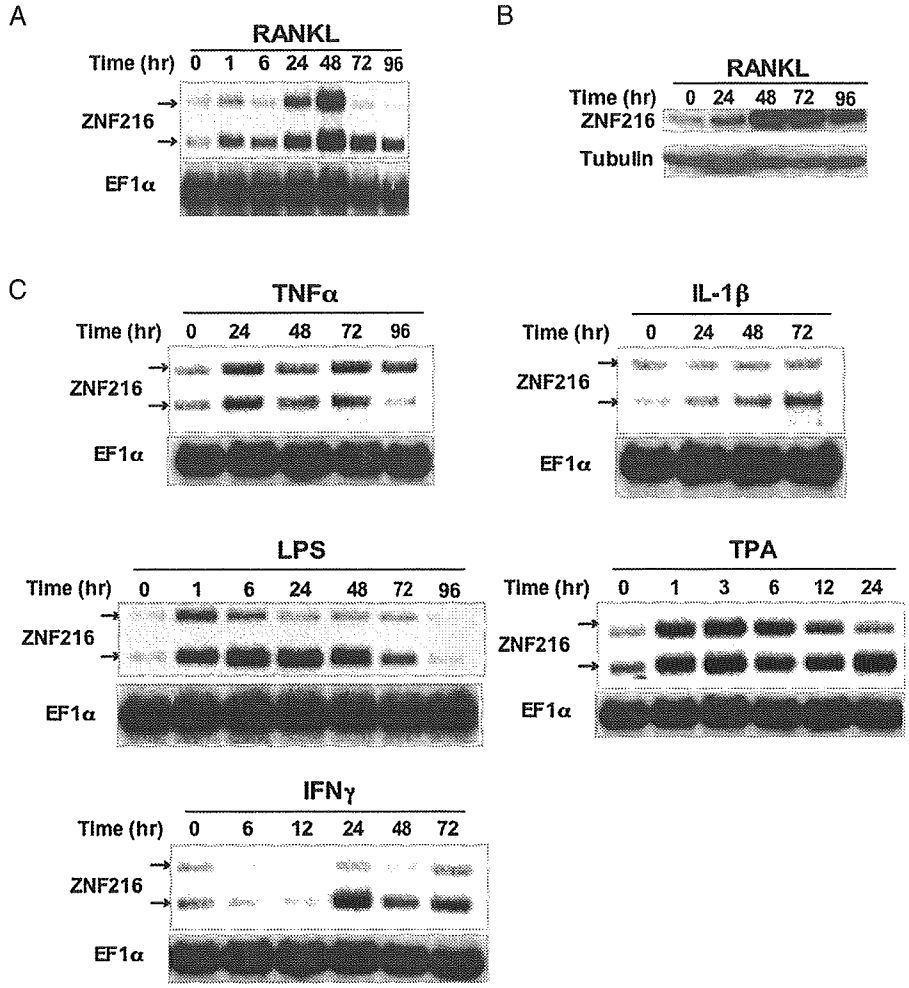

Figure 1: Expression of ZNF216. (A) The expression of ZNF216 is induced by RANKL. RAW264.7 cells were treated with RANKL (10 ng/mL) for the indicated time, and purified RNA was subjected to Northern blot analysis. The same membranes were reprobed for EF1α (elongation factor 1α) to control for loading. (B) Immunoblot analysis. The induction of ZNF216 protein is shown throughout a 96-hr time-course. The membrane was reprobed with tubulin antibody to control for protein loading. (C) Other proinflammatory cytokines or stimulators also induced ZNF216. Total RNA was prepared at the indicated time and probed for ZNF216 mRNA expression. The membrane was reprobed for EF1α as described above to control for loading.

pattern of the protein was well concordant with that of the RNA, the peak level of ZNF216 protein persisted long after 72 hr, when the RNA level had subsequently declined. RANKL-induced expression of ZNF216 was also observed in primary cultures of bone marrow macrophages (data not shown).

To examine whether expression of ZNF216 could be induced by other TNF superfamily cytokines, RAW264.7 cells were treated with TNFα. As expected,

TNFα up-regulated ZNF216, although not as much as RANKL (Fig. 1C). Both RANKL and TNFα activate a common signaling pathway through NF-κB and JNK with TNFR-associated factor (TRAF) family members (24). This intracellular pathway is known to be partially shared by those of IL-1β and LPS. As shown in Figure 1C, the expression of ZNF216 was also increased by treatment with both IL-1β and LPS. It is of interest that the expression was rapidly induced by LPS within 1 hr (Fig. 1C). In contrast, ZNF216 expression induced by IL-1β was rather weak. Thus, we hypothesized that activators of NF-κB or AP-1 might also induce ZNF216 expression. TPA, a potent activator of protein kinase C (PKC), activates NF-κB and AP-1 in rat 3Y1 fibroblasts and in the human gastric cancer cell line, MGC80-3 (25–27). As shown in Figure 1C, expression of ZNF216 was strongly induced by TPA in RAW264.7 cells. In addition, the antiviral cytokine, IFNγ, which is not known as an activator of NF-κB or AP-1, also up-regulated the expression of ZNF216 (Fig. 1C).

Ectopic Expression of ZNF216 in Osteoclast Differentiation

The ZNF216 protein is composed of 213 amino acid and contains both A20-like and AN1-like zinc finger domains (Fig. 2A). The A20-like zinc finger domain is a C2/C2 type zinc finger localized between amino acids 11–35 at the N-terminus (Fig. 2A). The AN1-like zinc finger domain is localized at amino acids 154–193 and contains the sequence CX2CX(9–12)CX(1–2)CX4CX2HX5HXC, which is similar to that of AN1, a ubiquitin-like protein in Xenopus laevis (28). To clarify the molecular function of ZNF216 in osteoclast differentiation, we generated RAW264.7 cells stably expressing either full-length or truncated forms of ZNF216, and in vitro osteoclastogenesis assays were performed. Comparable expression of ZNF216 and its mutants were confirmed by immunoblot analyses (Fig. 2A, right panel). Proliferation was not significantly affected by ectopic expression of ZNF216 mutants (not shown). Stably transfected RAW264.7 cells were seeded in 96-well plates and stimulated with RANKL for 48 hr. It is surprising that ectopic expression of full-length ZNF216 significantly suppressed TRAP-positive cell number compared with mock-infected RAW264.7 cells (Figs. 2B and C). By contrast, RAW cells expressing deletion mutations in either zinc finger domain (ΔN or ΔC) exhibited accelerated osteoclast differentiation monitored by TRAP (Figs. 2B and C). In particular, the C-terminal zinc finger domain truncated mutant (ΔC) dramatically promoted the expression of TRAP. Most of RAW264.7 cells expressing ΔC mutant were positive for TRAP, whereas mock-infected cells were only 25% TRAP positive (Figs. 2B and C). Ectopic expression of truncated mutants in RAW264.7 cells did not possess any TRAP activity without RANKL treatment, indicating that RANKL was required for the observed effects of on osteoclast differentiation (data not shown).